ASTRONOMY & ASTROPHYSICS
SUPPLEMENT SERIES

AUGUST **2000**, PAGE 341

Astron. Astrophys. Suppl. Ser. **145**, 341–350 (2000)

Achromatic interfero coronagraphy

II. Effective performance on the sky⋆

P. Baudoz[1], Y. Rabbia[2], J. Gay[1], R. Burg[3], L. Petro[4], P. Bely[4], B. Fleury[5], P.-Y. Madec[5], and F. Charbonnier[5]

[1] Observatoire de la Côte d'Azur, Dpt. Fresnel, UMR-CNRS 6528, BP. 4229, 06304 Nice Cedex 04, France
[2] Observatoire de la Côte d'Azur, Dpt. Fresnel, UMR-CNRS 6528, Av. Copernic, 06130 Grasse, France
[3] John Hopkins University, Baltimore, MD 21218, U.S.A.
[4] Space Telescope Science Institute, 3700 San Martin Drive, Baltimore, MD 21218, U.S.A.
[5] Office National de Recherche Aérospatiale, 29 avenue de la Division Leclerc, 92320 Châtillon, France

Received October 28, 1999; accepted May 9, 2000

Abstract. We report on the first observation run with the Achromatic Interfero Coronagraph (AIC) developed at Observatoire de la Côte d'Azur, France. Observations took place during Fall 97 at Observatoire de Haute Provence, France, with the 1.52 m telescope equipped at that time with adaptive optics. The Achromatic Interfero Coronagraph (AIC) is an imaging device providing the extinction of a star so as to detect and to image faint features of its close environment. Extinction results from a destructive interference process. Morphological features located as close to the star as the first angular Airy ring can be detected, thus breaking a limitation of the classical Lyot coronagraphs. The working spectral band was K. Observation results demonstrate the validity of the AIC approach with ground-based telescopes and illustrates close-sensing capabilities. After a short reminding of the principle of AIC, conditions of observations are reported and first results are discussed. Finally, limitations are evaluated and expected results are compared with effective performance.

Key words: methods: observational — instrumentation: interferometers — atmospheric effects — stars: binaries: close

1. Introduction

The difficulty of observing faint emissions in the close environment of bright objects like stars led astronomers to develop stellar coronagraphs. In the mid 1980's, coronagraphic masks placed in focal plane of ground based telescopes allow decreasing the flux ratio between the star and its close vicinity (see for example: Smith & Terrile 1984; Paresce et al. 1988). With the development of Adaptive Optic system (AO), a large amount of work has been done for improving the rejection rate of such coronagraphs. First developments were done with only tip-tilt correction (Walker et al. 1994; Nakajima et al. 1994). The latter coronograph drove to the discovery of Gl 105 C, a star close to the Hydrogen burning limit (Golimowsky et al. 1995) and to the discovery of the first brown dwarf: Gl 229B (Nakajima et al. 1995). More recently, Beuzit et al. (1997) placed a coronagraph behind the COME-ONE-PLUS adaptive optics system (50 actuators) and showed ratio of 10^5 accessible at 2 arcsec. At the beginning of 1999, Lowrance et al. (1999) and Schneider et al. (1999) obtained impressive results on dust disks around young stellar objects using the coronagraph installed with NICMOS on HST. But all coronagraphs cited above were designed on the basis of Lyot coronagraph (1939). In fact a typical layout for a Lyot coronagraph shows a mask in the focal plane that removes the major contribution of the star and a Lyot stop placed in the pupil plane so as to reduce light diffracted by the mask. However, to obtain good extinction with such a coronagraph, even with perfect incoming wavefront, the width of the mask can hardly be less than 6 times the width of the theoretical diffraction pattern (Malbet 1996). This characteristic prevents detection of close companions.

Recently new types of coronagraph has been proposed that show better theoretical extinction than the Lyot coronagraph and which do not prevent imaging as close as the first Airy ring: the Achromatic Interfero Coronagraph (Gay & Rabbia 1996) and the Phase Mask Coronagraph (Roddier & Roddier 1997). Both of them show large

Send offprint requests to: P. Baudoz,
e-mail: baudoz@obs-nice.fr

⋆ Based on observations collected at the 1.52 m of the Observatoire de Haute Provence, France.

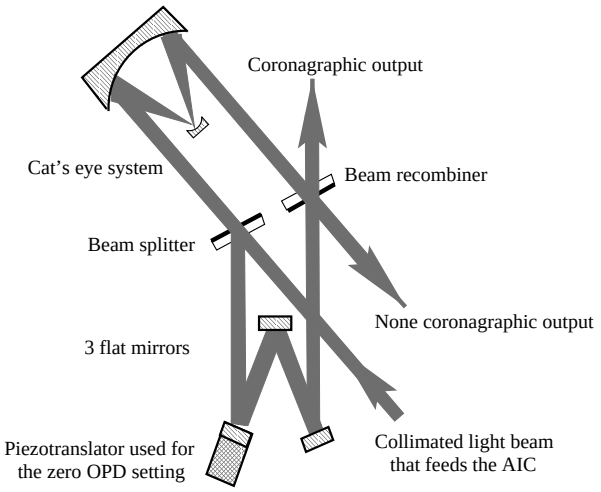

Fig. 1. Optical sketch of the experiment used for this observation run

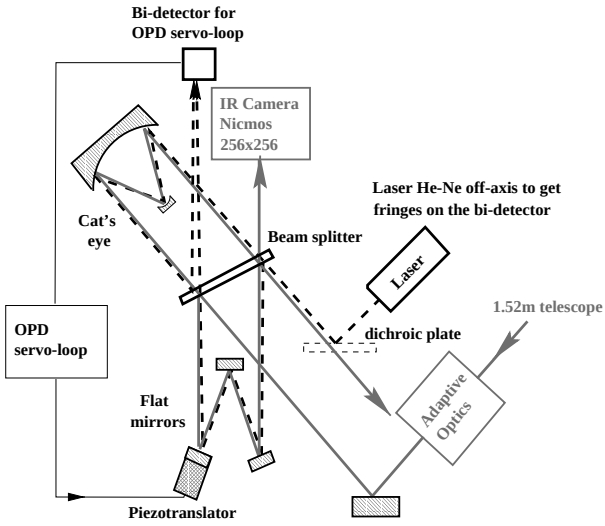

Fig. 2. Optical configuration for the observation run. Dotted lines stand for laser light beam used in OPD servo-loop while full lines stand for IR beam coming from telescope trough the AO system

reduction of the light of a star for a spaced-based telescope (Rabbia et al. 1997; Rabbia et al. 1998; Roddier & Roddier 1997). Moreover a study of the expected performance of the Achromatic Interfero Coronagraph (AIC) for ground based observation (Paper I: Baudoz et al. 1999) presents such encouraging assessments that it is inviting to carry on observations using a real device. In this perspective we have developed an AIC-prototype in order to confront theoretical estimates and effectives results. The goal of this paper is to present and discuss the results obtained with AIC on a 1.5 m telescope using AO. After a reminding of the principle of AIC and the description of the conditions of observation, first results are analysed. We eventually show the limitations of the AIC device effectively used for these observations and we compare expected performance with obtained results.

2. Principle of AIC

The optical sketch of Achromatic Interfero Coronagraph (AIC) is shown in Fig. 1. This coronagraph, described with more details in Paper I (Baudoz et al. 1999), is a modified Michelson interferometer. The main modification is the addition of a focus in only one arm of the interferometer. The focus is inserted so as to achieve a rotation of the pupil by 180 degres and so as to dephase the light wave by 180 degrees whatever the wavelength (achromatic dephasing). With such a set-up and when the Optical Path Difference (OPD) is kept at zero, the light from an unresolved on-axis source is utterly and achromatically nulled (Paper I). Any off-axis source escapes the interference process and gives two twin-images, symmetrically displayed with respect to the axis. The actual set-up of work is schematically described in Fig. 1. It performs the same nulling process than the basic device but rather looks like a double pass Michelson Fourier Interferometer (Connes & Michel 1975). Splitting of the incoming parallel beam and recombination of the separate beams are achieved by two separate halves of a unique coated plate, which are placed in appropriate position so as to avoid the use of a compensation plate. This configuration provides two output beams, one is the "destructive port" for imaging in coronographic mode, the other is the "constructive port" in which are found the photons removed from the coronagraphed output. The constructive port is used to control OPD by a servo-loop (Sect. 3.1).

3. Description of the observations

Observations reported here took place in october 1997 at the 1.52 m telescope of the Observatoire de Haute Provence (OHP). In this section we describe the instrumental configuration, the conditions in which this configuration had to work, the conditions driving the selection of the observed sources, and the observation procedure.

3.1. Instrumental configuration

The coudé focus of the 1.52 m telescope feeds an AO bench called BOA[1]. BOA is an 88 actuator system with a Shack-Hartmann wavefront sensor. Since BOA is not designed for infrared, its transmission in this spectral domain is not optimal (estimated to roughly 5%).

The working set-up actually used for observations is schematically described in Fig. 2. It differs from the one in Fig. 1 by adding a servo-loop to maintain the OPD

[1] BOA is an adaptive optics system developped at Office National d'Etudes et de Recherches Aerospatiales.

at zero. On the path of the none coronagraphic output, a laser beam is launched slightly off-axis and gives air-wedge fringes on a 2-element detector. The difference between the two outputs provides an error signal directly proportional to the OPD shift. A piezotranslator that moves a flat mirror placed in one arm of the AIC closes the OPD servo-loop. Optimisation of the close-loop parameters has been carried on in a quiet environment prior to the observations and led to a cut-off frequency of 2 Hz which has been judged sufficient for working in a quiet environment like the one expectable in a coudé room.

The camera, brought by the STScI group, is a Nicmos 3 array of 256×256 pixels equipped with a K band filter ($\lambda = 2.2$ μm, $\Delta\lambda = 0.4$ μm). The size of the pixel was 0.11 arcsec/pixel and the field of view was limited to 11 arcsec. The acquisition mode of the camera enables us to acquire 7 frames per second saved in cubes of 100 or 200 images. As a conservative value the global transmission of the focal assembly and of the telescope has been estimated to about 2%.

3.2. Specific conditions during observations

The conditions of turbulence during the observations were rather challenging. The Fried parameter r_0, estimated from the open-loop Shack-Hartmann data, varied from 1 to 10 cm. For the best 20% of the 10 nights of observation we derived a mean value for r_0 around 5 cm. Estimated outer scale L_0 varied from 2 m to 15 m with a mean value of 3 m. Since the value of the outer scale measured during the run is comparable to the telescope diameter the mean square residual of the phase for an estimated r_0 is indeed lower than predicted by the Noll theory (Noll 1976).

The coudé environment was not as quiet as expected. Vibrations and acoustic effects increased significantly the frequency and the amplitude of the OPD variations. The error signal from the OPD control-loop showed frequencies as high as 50 Hz and amplitudes as large as $\frac{\lambda_{\text{visible}}}{2}$. For the whole run, we have estimated a mean amplitude variation for the error signal of $\frac{\lambda_{\text{visible}}}{4}$ rms at the laser wavelength which gives in infrared (K band) an amplitude variation of $\frac{\lambda_{\text{IR}}}{15}$ rms.

In spite of many attempts we could not get rid of an important noise level in recorded images. The recorded images were also blurred with an additional "wave" signal. This high noise and the poor overall throughout of the focal assembly decreased the K magnitude limit for a single snapshot (exposure of 0.14 s) to $K = 4$ for a 3σ detection.

3.3. Selection of observed sources

Since this run was primarily intended to test AIC operating "on the sky" in ground based situation, known single stars and binary stars had to be considered. Single stars are useful to show the extinction capabilities of AIC, though they might have faint neighbouring features to extract. Binaries are used to evaluate capabilities regarding detection of companions and close-sensing around the central star.

Because of the large number of actuators in the AO, the visible magnitude needed to close the loop of the AO was limited to $V = 7$. The K magnitude has been limited to $K = 2$ in order to reach a convenient Signal to Noise Ratio in images needed to reliably evaluate departure from uncomplete nulling.

In the case of known binaries, two restrictions apply: the angular separation and the magnitude difference between the two components. The goal being to test the close-sensing capability down to a fraction of Airy radius separations (roughly 0.4 arcsec here), we limited our samples to binaries with separation below 2 arcsec. It turned out that only 3 binaries met the criteria: 5 Lac, HD 211073 and 72 Peg. The other observed stars are either single stars or stars suspected to be complex by Hipparcos.

3.4. Observation procedure

As in classical imaging techniques we need images of stars (target star and comparison star), skys, flat-fields and darks. We also need, as in typical AO observations, recording data for a comparison star under the same conditions than the target star. Such data allow to increase the detection capability by substracting the comparison pattern from the target pattern. In doing so, the shape of the halo is removed, not the noise, but nevertheless there is a gain since residual features with spatial frequencies comparable to those of the companion are then eliminated (residual effects of aberrations, averaged speckle noise).

A typical observation for a target star begins with calculation of the turbulence parameters with BOA in open loop. Then, BOA closes the loop and we put the star on-axis with the pointing mirror. The control of image position is not allowed by the acquisition mode of the camera. Therefore in order to ensure that no drift from differential atmospheric dispersion is happening (AO correction in visible with observation in IR), the observer has to periodically switch from blind acquisition mode to view mode, where pointing correction is performed if necessary. After images with star on-axis (nulled), images with star off-axis are recorded (twin images, no nulling). Then calibration of the extinction is achievable and photometry of a companion is available. Moving the telescope of half a degree, enables us to record sky emission close to the star. This procedure has to be repeated for comparison stars. Flat field is determined by recording images of a wide and uniform warm source illuminating the field of view of the camera (see Sect. 4.1).

4. Data reduction

4.1. Pre-processing

As usually done, sky background is substracted from the raw images which then are corrected from flat field effects. The flat-field has not been evaluated everyday. Therefore, some level variations might have occurred in the images from one observation to another one. Since high photometric precision was not whithin the goals of the observations we decided to tolerate such possible fluctuations, even though they might affect the performance in extinction.

As described in Sect. 3.2 recorded images were blurred with an additional "wave" signal. A specific computer program has been devoted to remove this "wave" signal. The noise variances in raw images have then been improved by a factor of two.

4.2. Image selection

Several effects prevent a full achievement of the nulling process. The AO system does not completely remove wavefront distorsions (tip-tilt effect which randomly moves the image off-axis proved to be the more severe), the OPD is not perfectly maintained at zero and some drift in image position (due to atmospheric dispersion) might happen. These effects result in residual unwanted light variable in shape and intensity.

Therefore it seems that the only way to limit the residual light is to rely on "good images" and thus a selection must be made. Since the residual light lies around the axis and is enhanced by the wavefront degradations the selection criterion is based on the intensity measured in a box of 9×9 pixels (1 arcsec square) centered on the position of the AIC axis: the less the energy in the box, the better the image. On one hand, the frequency of the tip-tilt effect and the frequency of the pointing drifts were low enough to be freezed by the frame rate of the camera (7 Hz). On the other hand, OPD perturbations proved to go beyond the freezing capability of the camera and no images were obtained with low OPD perturbations.

We have built 10 quality-classes, each containing images exhibiting the same residual energy in the box. Depending on the seeing and in spite of AO corrections, some data cube contain images which energy level in the box is larger than the one of the lowest quality class. As a consequence the number of frames per class is different from one class to another and from one star to another.

5. Effective performance of AIC

The efficiency of the coronagraph can be measured by comparing images of the same object respectively on-axis and off-axis (Fig. 3). When the star is set off-axis by 4 or 5 times the distance of the first Airy ring (this is about 2 arcsec here) the nulling process no longer applies. Thus as shown in Fig. 3 (image on the left), the photometry of the star is available through the twin images (the summed energy in the twin images is half the energy reaching the beamsplitter). When the star is on-axis a halo of residual energy appears (as shown in Fig. 3). Basically the ratio of the energy in the residual halo to the incident energy determines the extinction capabilities, and this led to the criterion: normalised integrated residual energy. In the following we use this criterion to evaluate the effect of AIC on AO typical images. We also compare two reduction techniques for AIC images and we show how AIC reaches a higher close-sensing capability than does the Lyot coronagraph.

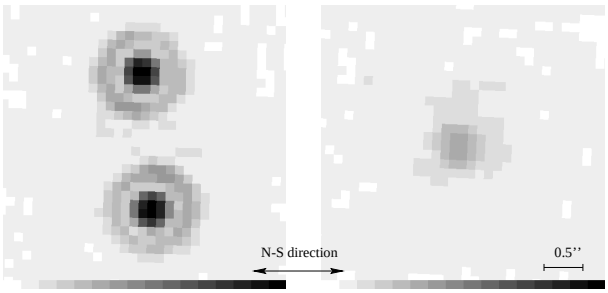

Fig. 3. Image of a star off-axis and on-axis. The scale is linear and is the same for the 2 images

5.1. Integrated residual energy

Let's call w_0 the total energy that hits the AIC beamsplitter (i.e., the total energy collected on the star by the telescope taking into account optical transmission before the AIC). This quantity is twice the total energy from the twin images. From the derivation in Paper I, the normalised integrated residual energy is given by:

$$g_J = p_J . \left(\frac{D}{r_0(\text{vis})}\right)^{\frac{5}{3}}$$

where D is the diameter of the telescope, r_0 is the Fried parameter in the visible and p_J is a coefficient depending on J, the index of the last Zernike polynomial corrected.

In Fig. 4 we plot the value of the integrated residual intensity g_J versus the factor $\frac{D}{r_0(\text{vis})}$ for a sample of data collected during the observation run. The filled circles stand for g_J measured when adding the whole set of images of a star and the squares stand for g_J measured when adding only selected best images of a star. The selected best images for each target represent between 8% and 15% of the total number of images (in Sect. 4.2 we have explained why the number of images varies from quality-class to another). The best regression lines (whole set and selected set) are also drawn. They yield respective estimates of p_J via the expression: $g_J = p_J . \left(\frac{D}{r_0(\text{vis})}\right)^{\frac{5}{3}}$. For the whole

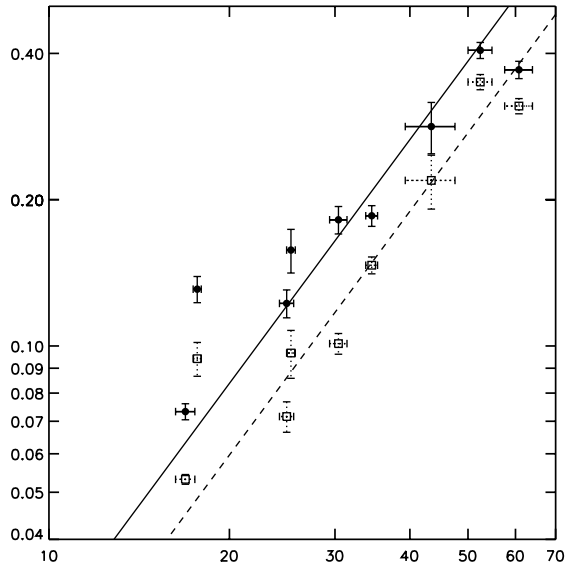

Fig. 4. residual energy rejection rate (g_J) in vertical versus $\frac{D}{r_0(\mathrm{vis})}$ in horizontal. Filled circles stand for calculation with the whole set of images of a star. The squares use only selected best images of a star. The error bars show the 1 σ dispersion

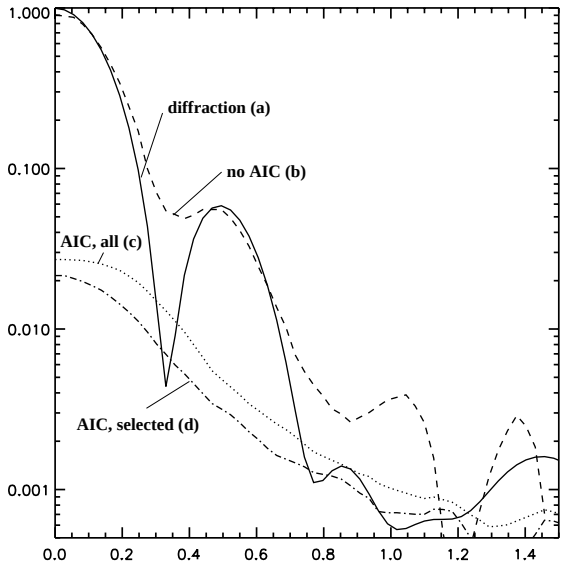

Fig. 5. Mean radial profile of a star (vertical) versus angular separation (in arcsecond). **a)** theoretical diffraction pattern. **b)** profile without AIC. **c)** profile with AIC and the whole set of images of the star. **d)** profile with AIC and a selection of the best images of the star

set of images we find $p_J = 0.009$ (solid line in Fig. 4) while for the selected images $p_J = 0.0065$ (dashed line in Fig. 4). The theoretical coefficient p_J for BOA is 0.0025. In comparison the AO acts as if it was an AO completely efficient up to radial mode $N = 7$ (36 polynomials). The error bars show the 1σ dispersion. Vertically the precision has been estimated taking into account the temporal variation of the extinction and of the total energy collected w_0. Horizontally the limitations come mainly from the temporal variation of the r_0 during the observations. This variation of r_0 is estimated from the BOA measurements taken on each star.

5.2. Radial profiles of residual energy

We have to take into account the shape of the halo because it makes the detection capability variable with the location of the image of a companion. In addition we want to visualize the shape of the halo of residual light effectively obtained from the observational data. For that matter we consider the case where AIC has given its best results (here $\frac{D}{r_0(\mathrm{vis})} = 17$). In Fig. 5 we show profiles of the normalised flux pertaining respectively to the diffraction pattern of the telescope, central obscuration taken into account (profile a), to the observed image without coronagraph and where AO provides a Strehl Ratio of 90% in K band (profile b, 150 images), to the residual light averaged over the whole set of images (profile c, 1200 images) and to the residual light averaged over the set of selected best images (profile d, 150 out of 1200 images). In Paper I, we suggested that the residual energy is spread over an extended halo, what is effectively found from our data. Unsurprisingly the coronagraphed profile from the selected set is lower and less extended than the profile from the whole set. This change brings in a reduction of the integrated energy from 7.5% to 5.5% that is a lowering factor of 0.73 and reduces the height of the central peak from 2.6% to 2.1% that is a lowering factor of 0.8. Those numerical figures illustrates the interest of a selection process and the presented profiles show where and how the situation is thus improved.

However, we should have observed a depression at the origin in the coronagraphed profiles, as expected from the analysis in Paper I. and this is clearly not confirmed by our profiles from data. This discrepancy between expected and observed profiles is well explained on the theoretical ground by unstabilities affecting OPD (see Paper I) and this situation has been clearly met in our observations, as commented in Sect. 3.2 (specific conditions of observation). In addition, the central hole expected from the theoretical extinction profile can yield full extinction only over an area smaller than the pixel size. Therefore a small fraction of the residual energy is constantly present and prevents the "full darkening" of the central pixel. This also contributes to the observed central peak (but significantly less than OPD variations do).

5.3. Magnitude difference reachable from raw data

In this section, to demonstrate more quantitatively the effect of AIC, we compare the magnitude difference (ΔK)

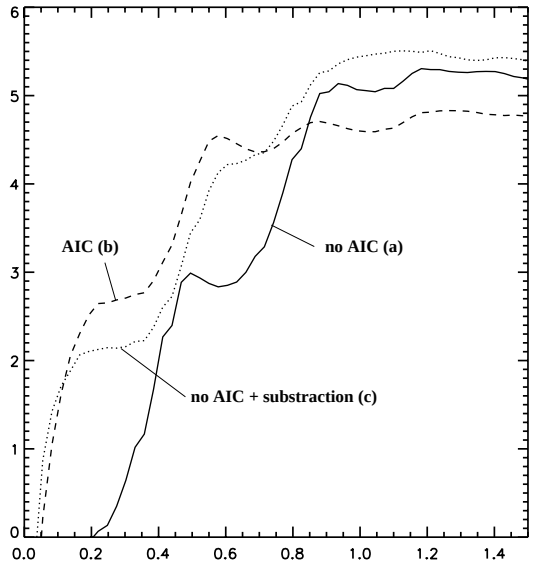

Fig. 6. Detection capabilty in magnitude versus separation with the main star (horizontal scale). curve a and b respectively ΔK accessible without and with AIC (both raw data). Curve c is the ΔK accessible without AIC with substraction of a comparison star (also without AIC)

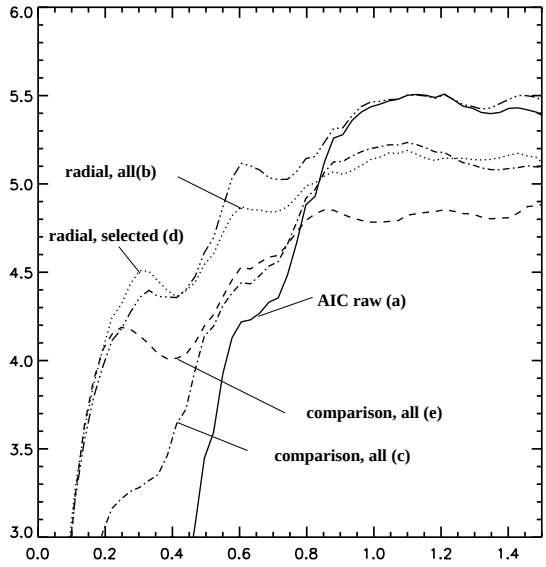

Fig. 7. Vertically: magnitude difference accessible. Horizontally: separation with the main star in arcseconds. See text for details

detectable at a given angular resolution with AIC and without AIC. The ΔK values correspond to the lower limit of the detectable flux of the companion at the level of 3σ. The noise is evaluated by integration of the energy over a $0.36'' \times 0.36''$ patch (Paper I, Close et al. 1998) and this patch is radially moved to determine the variation of the noise level versus the angular distance to the axis. The total flux of the companion is determined by the energy enclosed within the patch centered on each image of the companion. One must notice that the total flux recorded from the companion depends also on the angular separation but the effect of the dependency is visible only close to the star (see Paper I). Roughly AIC diminishes the flux from the companion when this one is closer to the star than $0.18''$ while there is practically no attenuation beyond.

In Fig. 6 we show the ΔK accessible from raw data without and with AIC (curve a curve b) for typical conditions of turbulence ($\frac{D}{r_0(\mathrm{vis})} = 25$). Substracting the comparison star from the target star profile (both obtained without AIC) yields the curve c. It is apparent from the graph that curve b and c correspond to nearly the same detection sensitivity, what means that working with raw data of AIC is as good as working with "cleaned" data without AIC. Such a situation shows that processing raw data is necessary to improve the detectivity and ultimately to recover the expected performance.

5.4. Comparison between two reduction methods

In this section we compare the ΔK given by 2 different reduction processes:

1. substracting a comparison star (comparison process);
2. substracting the mean radial profile (radial process).

Substracting the mean radial profile is possible as soon as the correction by AO is good enough (Strehl Ratio (SR) larger than 50%) what is the case here. In Fig. 7 the ΔK is calculated as described in Sect. 5.2. In this figure we show for comparison the ΔK detectable from raw data (curve a in Fig. 7). The curves b and c (Fig. 7) shows the ΔK accessible respectively for the radial process and for the comparison process (both curves uses the whole set of images available for the target star and the comparison star).

For this configuration (star magnitude, number of frames, exposure time and high noise of the camera), the detectability is limited to $\Delta K = 5$ beyond 1 arcsec separation. We can note that close to the star the radial process is more efficient than the comparison process. In fact, close to the star the shape of the profile is very similar to the theoretical radial profile (large SR). This leads to a shape of diffraction pattern very similar to the theoretical one. Since this pattern is radial the radial process works well. Besides, the comparison process is not very efficient close to the star because of the possible incidental on-axis pointing shift between the target star and comparison star. This slight angular shift makes the respective mean patterns unequal close to the axis, and limits the efficiency of the comparison process.

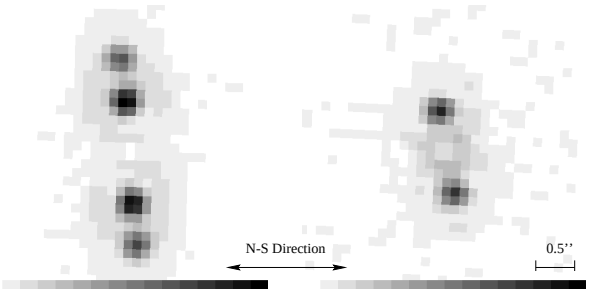

Fig. 8. Image of the double star HD 211673 off-axis and on-axis. Separation of the two components is 1.4 times the distance of the first Airy ring (0.53 arcsec). Difference of magnitude in K is estimated at about 0.36

In the comparison process used far from the star the detectivity is reduced because noises from target and comparison contribution are added, then decreasing the detectable ΔK.

As described in Paper I one specific interest of AIC is its capabilities of detection close to the star. Then to study the efficiency of the AIC close to the star, we calculate the ΔK accessible with a selection of the best images of both target and comparison star for the two reduction processes we are interested in (curve d for radial process and curve e for comparison process, both in Fig. 7). When using the selection of best images we keep about 150 images while with the whole set of data we use 900 images.

Using a reduced number of images tends to decrease the detectable ΔK far from the star. Conversely, close to the star this ΔK is increased because the selection tends to favor images with the highest wavefront quality which results in removing residual energy around the axis first.

We have shown in this section that the selection of images helps increasing detectability of faint structures close to the axis. The use of reference stars does not seem necessary from the averaged radial curves we show. However, when searching for faint structures, one can be misled by fixed speckles mainly coming from aberrations in the wavefront sensor unit or in the optical set-up standing between the AO output beamsplitter and the AIC entrance. Reference sources are then still necessary.

5.5. Close-sensing capabilities

To evaluate the close-sensing capability of AIC we have recorded images of several double stars of various angular separations. In Fig. 8 we present the case of the double star HD 221673 (72 Peg) where the separation is 1.4 times the angular distance of the first Airy ring (0.53 arcsec). From the recorded images (K band) we have estimated the magnitude difference between components at $\Delta K = 0.36$. Hipparcos (ESA 1997) gives a difference of magnitude of $\Delta Hp = 0.46$ (Hipparcos magnitude Hp, visible-near infrared, Martin 1996).

Though, for this star, the magnitude difference to deal with is not very challenging it shows how AIC works. A more challenging star is HD 211073 for which we have to face magnitude differences $\Delta Hp = 3.46$ (Hipparcos Catalogue ESA 1997), $\Delta R = 2.9$ and $\Delta I = 2.2$ (Ten Brummelaar et al. 1996) and a separation of $0.4''$ (Hartkopf et al. 1996). For this star the best results have been obtained with the radial process, because the superimposition of target star and comparison star was not good enough. No faint companion appears clearly but at the position given by Hipparcos Catalogue (ESA 1997) and Hartkopf et al. (1996) two symmetrical bright speckles appear at the level of the residual fixed speckle noise. The difference of magnitude derived from the level of these speckles is $\Delta K = 6.4$. This result is not in agreement with a low mass companion hypothesis derived by Ten Brummelaar et al. (1996).

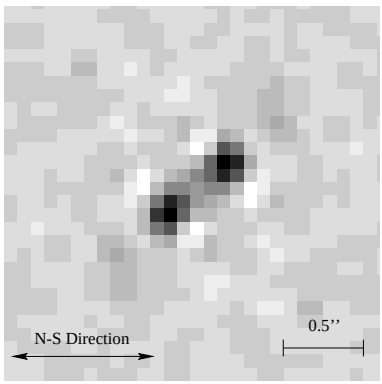

Fig. 9. Image of the faint component of the double star HD 213310. Separation of the two components is the third of the diffraction limit. Difference of magnitude in K is estimated at about 3.5

To show that the AIC can detect companions as close to the star as half of the distance of the first Airy ring we observed the star HD 213310 (5 Lac). The two components of the star are only about 0.11 arcsec appart (one third of the first dark Airy ring). This companion is too close to the star to be resolved by the telescope, but as shown in Paper I, it should be possible to detect this companion with AIC. Figure 9 shows that this possibility is effective and that a sensing of the environment as close as a third of the Airy angular radius has been achieved with AIC. Let us give few comments regarding this point. The image of a companion closer than the first Airy ring appears as two spots symmetrically located at 0.6 times the distance of the first dark Airy ring (Paper I), i.e. 0.22 arcsec here, even if the true separation is different. Actually the true separation governs the apparent flux, not the location of the image. The bright spots (twin images) from HD 213310 effectively appear at the expected location, with a Signal to Noise (SNR) of 5 (Fig. 9). Both the radial and comparison processes give the same result. The intensity ratio between the main star and these spots is 42. From this estimate and taking an average separation of 0.11 arcsec (Hartkopf et al. 1996) a magnitude difference $\Delta K = 3.5 \pm 0.5$ is found. The uncertainty ΔK comes from the uncertainty regarding the angular separation and also

from the low level of detection (SNR = 5). This magnitude difference is consistent with the spectral types of the 2 stars. Markowitz (1969) gives for these stars M0II+B8V (see also Ginestet et al. 1997 for more references on this star).

Classical Lyot coronagraph can not image a companion so close to the main star. Actually, the masks used in Lyot-type coronagraphs cover 2 to 10 times the distance of the first Airy ring (Malbet 1996) and most of the time they cover 4 or 5 times this distance (Beuzit et al. 1997; Mouillet et al. 1997). As we have shown in this section, AIC can image the faint companion at one third of this distance (first dark Airy ring).

6. Limitations regarding detection capability

6.1. Nature of the various limitations

In order to improve the performance of AIC one wants to know the relative weights of the various limitations. Far from the star the main limitation comes from the camera noise but close to the star it is the residual energy from the star which decreases the detectivity. This latter limitation is the most annoying since it tends to cancel a specific advantage of AIC (close sensing capability) and since AO correction is particularly efficient close to AIC axis (Paper I). This residual energy comes from the corruption of the wavefront by optical aberrations. These aberrations can be divided into the optical aberrations before the AIC (residual turbulence through the AO, fixed aberrations in the wavefront sensor unit or in the optical set-up after the AO beamsplitter), the optical aberrations inside AIC, and the OPD variations (which could be also included into the aberrations inside AIC).

6.2. OPD variations

From laboratory tests, we know that the contributions of the various aberrations inside AIC amount to less than 0.5% of the integrated energy without AIC. Besides, we have already said that OPD residual fluctuations were exceedingly large, as a result of the unexpected vibrations of the building structure and of numerous acoustic perturbations (rms variation about $\frac{\lambda}{15}$ in IR).

In Appendix A: we show that the main contribution to the residual energy of AIC comes from these OPD variations. The mean intensity in the output image plane takes the form:

$$I(\boldsymbol{\rho}) \approx RT \left[< |2 \sum_{\text{odd},i=J}^{\infty} a_i \hat{Z}_i(\boldsymbol{\rho})|^2 > + < d^2 |\hat{Z}_1(\boldsymbol{\rho})|^2 > \right]$$

with

$$\hat{Z}_i(\boldsymbol{\rho}) = \pi\sqrt{n+1}(-1)^{(n-k)/2} i^{-k} \frac{2J_{n+1}(2\pi\rho)}{2\pi\rho} \exp(ik\theta).$$

As explained in Paper I, and as appearing in the formulae, the summation in the first term applies only on Zernike polynomials with odd radial degree. Since $J_n(\rho)/\rho = 0$ for $\rho = 0$ for $n > 1$, the summation in the first term is null for small ρ, and there is no contribution from the first term on the axis of AIC. The observed radial profile of the residual energy coming out of AIC shows a central peak (see Fig. 5). The second term explains this a priori unexpected shape, and is much likely to be the major cause yielding the central peak, eventhough the finite pixel size contribute to this central peak (see Sect. 5.2). In other words when $RT. < d^2 >$ is not null the central pixel is not utterly dark. Taking this into account we calculate the coefficient $RT. < d^2 >$ that is a weighting factor to apply to the theoretical diffraction pattern without coronagraph. The coefficient $RT. < d^2 >$ for our data exhibits a mean value of 2.5% and varies between 1.5% to 3% from one star to another one. This is consistent with the variation of $\frac{\lambda}{15}$ rms in IR observed during the run. One must keep in mind that about 0.5% of the integrated energy comes from the AIC aberrations but for such small aberrations the contribution on the axis is negligible.

7. Comparison between effective and expected performance

From the mirror commands that were recorded in closed loop, the BOA group is also able to calculate the residual variances of the Zernike coefficients. This numerical calculation, that uses an atmospheric model, has been performed up to $J = 45$ assuming that the wavefronts distortions corresponding to higher Zernike orders are not corrected. In fact the reconstruction of the coefficients for $J > 45$ is not significant because their values are comparable with the ones of the reconstruction noise.

From the values of the variances derived from the wavefront sensor data, we are able to simulate radial profiles given by AIC (Paper I). The simulation takes into account the spectral bandwith and the telescope obstruction. The observed profiles cannot be readily compared to the simulated ones, because of the energy contribution from the OPD variations. In order for the comparison to make sense we have substracted a diffraction pattern weighted by $RT. < d^2 >$ from the observed profile which practically yields the profile we should have observed with AIC free from OPD fluctuations. In Figs. 10, 11, 12 we compare simulated and obtained profiles with and without AIC for three different conditions of turbulence (respectively $\frac{D}{r_0(\text{vis})} = 17$, $\frac{D}{r_0(\text{vis})} = 43$, $\frac{D}{r_0(\text{vis})} = 52$). From these figures we see that there is a good agreement between the simulated profiles and the "observed-OPD removed" profiles, which shows the relevance of the analysis appearing in Paper I and regarding performance of AIC under turbulence. Then, when the mean values of the residual variances for a given AO are available, we can predict realistic and reliable profiles of the residual energy distribution at the output of AIC.

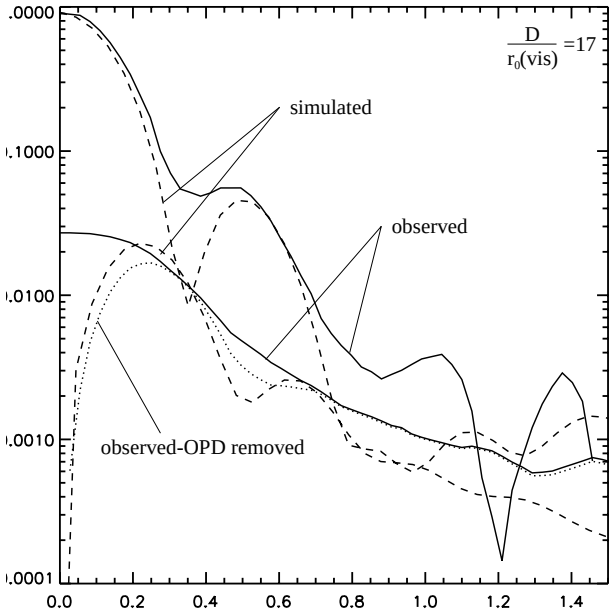

Fig. 10. Mean radial profiles for $\frac{D}{r_0(\mathrm{vis})} = 17$. Full lines: recorded profiles with and without AIC (no selection of images). Dashed lines: simulated profiles with and without AIC. Dotted line recorded profile with AIC with substraction of the profile of a diffraction pattern weighted by $RT. < d^2 >$. Horizontal scale: arcseconds on the sky

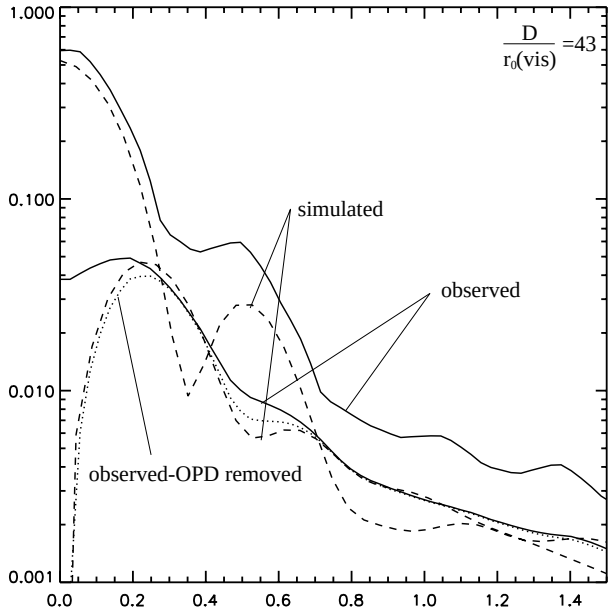

Fig. 11. Mean radial profiles for $\frac{D}{r_0(\mathrm{vis})} = 43$. Full lines: recorded profiles with and without AIC (no selection of images). Dashed lines: simulated profiles with and without AIC. Dotted line recorded profile with AIC with substraction of the profile of a diffraction pattern weighted by $RT. < d^2 >$. Horizontal scale: arcseconds on the sky

8. Conclusion

In this Paper we have reported observations and results of a first test run with AIC on ground-based telescope and we have shown the interest of this type of coronagraph. In particular, we have achieved from raw data, a clear detection of a companion close to a star at an angular distance of less than the Airy angular radius and fainter than the star by $\Delta K = 3.5$. This close-sensing capability has been demonstrated with the observation of 72 Peg and 5 Lac, and this capability can be enhanced by means of an appropriate post-processing of the raw data. AIC takes full advantage of the theoretical angular resolution of the telescope. Thus, it is clear that using AIC on large telescopes equipped with Adaptive Optics corrections will lead to a very-close sensing at a level better than set by the diffraction limit. With AIC the effect of the corrections by adaptive optics is to remove residual light from the coronagraphed image. The correction affects the center of the field first and gradually enlarges this "cleaned area" as the number of corrected Zernike modes is increased. This is another interest of AIC: even with a limited number of corrected modes the center of the image is "cleaned" first.

The AIC device used for these observations was a prototype undergoing exceedingly large and fast OPD variations, which has severely limited the detection capability. For example our evaluation (Paper I) of the performance in case of uncomplete correction by AO, falls short by nearly two magnitudes with respect to the observations, and this can be explained mainly by the OPD variations. Both the size of the prototype and its sensitivity to OPD variations make it unadequate for observations on large telescopes (for which, generally speaking, only Cassegrain focus are equipped with AO). A new AIC device which is compact, has low weight and has robust OPD balance has been developed at Observatoire de la Côte d'Azur, France for observations on large telescopes. The AO system is the key point for the efficiency of AIC since working with the best wavefront is the condition required for reaching the best performance. No doubt that coupling AO and laser star will significantly increase the capabilities of AIC for ground-based observations, even though the ultimate nulling performance will be reached by installing AIC on a space-based telescope.

Appendix A: Contribution of the aberrations to the residual energy on the axis of the AIC

We calculate here the mean intensity behind AIC with an OPD error:

$$I(\boldsymbol{\rho}) = RT < |\mathrm{TF}[P(\mathbf{r})\exp(i\phi(\mathbf{r}))]_{\boldsymbol{\rho}} - \mathrm{TF}[P(\mathbf{r})\exp(i\phi(-\mathbf{r}))\exp(id)]_{\boldsymbol{\rho}}|^2 > .$$

We approximate $\exp(ia) \approx 1 + ia$ because the fluctuations of the turbulent phase are small because the first aberrations are corrected by the AO. The fluctuations of the OPD are also small (about $\frac{\lambda}{15}$ in IR).

$$I(\boldsymbol{\rho}) \approx RT < |i\mathrm{TF}[P(\boldsymbol{r})(\phi(\boldsymbol{r}) - \phi(-\boldsymbol{r}) - d)]_{\boldsymbol{\rho}}|^2 > .$$

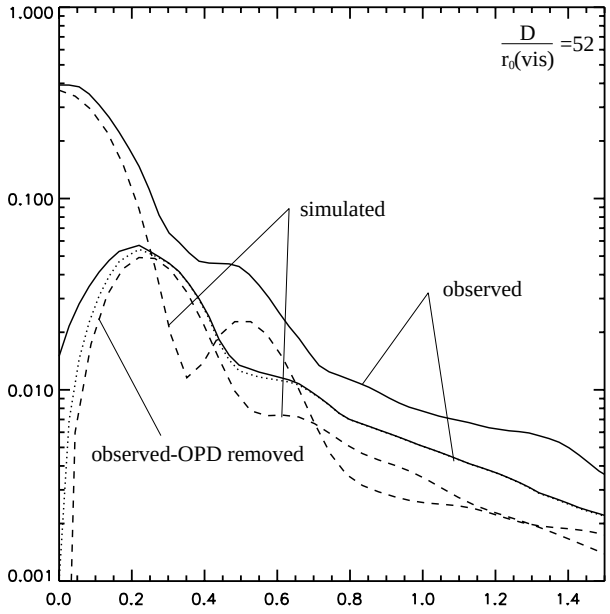

Fig. 12. Mean radial profiles for $\frac{D}{r_0(\mathrm{vis})} = 52$. Full lines: recorded profiles with and without AIC (no selection of images). Dashed lines: simulated profiles with and without AIC. Dotted line recorded profile with AIC with substraction of the profile of a diffraction pattern weighted by $RT. < d^2 >$. Horizontal scale: arcseconds on the sky

We develop the phase errors in Zernike polynomials (Noll 1976, Paper I). The even Zernike polynomials are removed because of the rotation of the pupil in one arm and the sum is only done on odd radial polynomials.

$$I(\boldsymbol{\rho}) \approx RT < |\mathrm{TF}[2i \sum_{\mathrm{odd},i=J}^{\infty} a_i Z_i(\boldsymbol{r}) - id P(\boldsymbol{r})]_{\boldsymbol{\rho}}|^2 > .$$

Remembering that $P(\boldsymbol{r}) = Z_1(\boldsymbol{r})$ and calling $\mathrm{TF}[Z_i(\boldsymbol{r})]_{\boldsymbol{\rho}} = \hat{Z}_i(\boldsymbol{\rho})$

$$I(\boldsymbol{\rho}) \approx RT < |2i \sum_{\mathrm{odd},i=J}^{\infty} a_i \hat{Z}_i(\boldsymbol{\rho}) - id\hat{Z}_1(\boldsymbol{\rho})|^2 > .$$

As

$$\hat{Z}_i(\boldsymbol{\rho}) = \hat{Z}_{nk}(\rho,\theta) = \pi\sqrt{n+1}(-1)^{(n-k)/2} i^{-k} \frac{2J_{n+1}(2\pi\rho)}{2\pi\rho} \exp(ik\theta)$$

depends on i^{-k} the term $2i \sum_{\mathrm{odd},i=J}^{\infty} a_i \hat{Z}_i(\boldsymbol{\rho})$ is real while the term $id\hat{Z}_1(\boldsymbol{\rho})$ is imaginary.

Then the cross values are null and we obtain:

$$I(\boldsymbol{\rho}) \approx RT \left[< |2 \sum_{\mathrm{odd},i=J}^{\infty} a_i \hat{Z}_i(\boldsymbol{\rho})|^2 > + < d^2 |\hat{Z}_1(\boldsymbol{\rho})|^2 > \right] .$$

The first term is the same as the one found in Paper I and gives no light contribution on the axis of the AIC. The second term is then the term that explains the residual peak found on the axis of the AIC.

Acknowledgements. We are grateful to the Observatoire de Haute Provence staff and the Office Nationale d'Étude et de Recherche Aérospatiale staff. Part of this work has been performed using the computing facilities provided by the program "Simulations Interactives et Visualisation en Astronomie et Mécanique (SIVAM)".

References

Baudoz P., Rabbia Y., Gay, 2000, A&AS 141, 319
Beuzit J.-L., Mouillet D., Lagrange A.-M., Paufique J., 1997, A&AS 125, 175
Close L.M., Roddier F., Roddier C., Graves J.E., Northcott M., Potter D., 1998, Proc. SPIE 3353, 406
Connes P.M.G., 1975, Appl. Opt. 14 (9), 2067
ESA 1997, The Hipparcos and Tycho Catalogues, ESA SP-1200
Gay J., Rabbia Y., 1996, C.R. Acad. Sci. Paris 322, Serie IIb, 625
Ginestet N., Carquillat J.M., Jaschek C., Jaschek M., 1997, A&AS 123, 135
Golimowski D.A., Nakajima T., Kulkarni S.R., Oppenheimer B.R., 1995, ApJ 444, L101
Hartkopf W.I., McAlister H.A., Mason B.D., 1996, Third Catalogue of Interferometric Measurements of Binary Stars, http://www.chara.gsu.edu/DoubleStars/Speckle/intro.html
Lowrance P.J., McCarthy C., Becklin E.E., Zuckerman B., Schneider G., Webb R.A., Hines D.C., Kirkpatrick J.D., Koerner D.W., Low F., Meier, Rieke M., Smith B.A.R., Terrile R.J., Thompson R.I., 1999, ApJ 512, L69
Lyot B., 1939, MNRAS 99, 580
Markowitz A.H., 1969, Ph.D. Thesis, Ohio State Univ.
Martin C., 1996, Ph.D. Thesis, Université Nice Sophia-Antipolis
Malbet F., 1996, A&AS 115, 161
Mouillet D., Lagrange A.-M., Beuzit J.-L., Renaud N., 1997, A&A 324, 1083
Nakajima T., Durrance S.T., Golimowski D.A., Kulkarni S.R., 1994, ApJ 428, 797
Nakajima T., Oppenheimer B.R., Kulkarni S.R., Golimowski D.A., Matthews K., Durrance S.T., 1995, Nat 378, 463
Noll R., 1976, J. Opt. Soc. Am. 66, 207
Paresce F., Burrows C., Horne K., 1988, ApJ 329, 318
Rabbia Y., Baudoz P., Gay J., 1998, in: The Next Generation Space Telescope: Science Drivers and Technological Challenges, 34th Liège Astrophysics, p. 279
Rabbia Y., Gay J., Baudoz P., Manghini C., Vaillant J., 1997, in: Scientific Satellites Achievements and Prospects in Europe, ESA/AAAF, p. 354
Rigaut F., Salmon D., et al., 1998, PASP 110, 152
Roddier F., Roddier C., 1997, PASP 109, 815
Schneider G., Smith B.A., Becklin E.E., Koerner D.W., Meier R., Hines D.C., Lowrance P.J., Terrile R.J., Thompson R.I., Rieke M., 1999, ApJ 513, L127
Smith B., Terrile R., 1984, Sci 226, 1421
Ten Brummelaar T.A., Mason B.D., Bagnuolo W.G., Hartkopf W.I., McAlister H.A., Turner N.H., 1996, AJ 112, 1180
Véran J.-P., Rigaut F.J., Rouan D., Maitre H., 1997, J. Opt. Soc. Am. A 14 (11), 3057
Walker G.A.H., Walker A., Racine R., Fletcher J.M., McClure R.D., 1994, PASP 106, 356